14.7 EVOLUTION OF TANGENTIAL AND RADIAL FLOWS OF TYPHOON NARI (2001) AT LANDFALL

Ming-Jen Yang*, Tai-Chi Chen Wang, and Ching-Yi Weng
National Central University, Chung-Li, Taiwan

1. INTRODUCTION

Although there have been many observational and modeling studies of tropical cyclones (TCs), our understanding on the evolution of TC's tangential and radial flows during the landfall process is rather limited. Gradient-wind balance (GWB) assumption for the tangential wind has been widely used in theoretical studies of TCs (Shapiro and Willoughby 1982; Emanuel 1986). Schubert and Hack (1983) used the transformed Eliassen-balanced equation to describe the response of TC's secondary circulation (vertical velocity and radial wind) to the latent heating and friction.

Both sounding observations from LaSeur and Hawkins (1963) and aircraft measurements from Willoughby (1990, 1991) found that the GWB model is a good approximation to the azimuthally-averaged tangential winds in the inner-core region for flows above the marine boundary layer (MBL) and below the upper outflow layer. On the other hand, Gray and Shea (1973) documented systematic gradient unbalanced flows in the eyewall, especially near the radius of maximum wind (RMW). Zhang et al. (2001; hereafter referred to as ZLY) performed the absolute angular momentum (AAM) and radial momentum budgets, using their high-resolution simulation (with horizontal grid spacing of 6 km) of Hurricane Andrew (Liu et al. 1997), and have reconciled the controversy between Gray and Shea (1973) and Willoughby (1990). ZLY indicated that their conclusions are both correct for the levels of observations they analyzed, because of significant differences in the agradient forces and flows between the layers near the top of the MBL and the layers above. However, these studies are only for oceanic TCs, and it remains unknown whether the GWB model is still applicable when a TC makes landfall. It is also not clear how the radial flow will evolve as a TC impinges steep terrain, such as the Central Mountain Range in Taiwan (with the highest mountain peak of 4 km).

As indicated by ZLY, the GWB model for the primary circulation is important to understand TC's secondary circulation. The gradient wind imbalance is required to determine the intensity and structure of secondary circulation, which would in turn cause the intensity change of the primary circulation. Radial inflows (outflows) tend to increase (decrease) the magnitude of tangential winds in the eyewall under the constraint of AAM conservation. On the other hand, the radial outflow in the eye plays an important role in transporting the air mass from the inner-core region outward to reduce the central pressure, strengthen the storm, and then intensify the tangential wind (Liu et al. 1999). While the TC vortex over the ocean has been extensively studied in the context of balanced dynamics, it is still uncertain to what extent the GWB is still valid for a landfalling TC, and how the unbalanced flows are generated and distributed in the inner-core region as a TC encounters steep topography.

Typhoon Nari struck Taiwan on September 16, 2001; it brought heavy rainfall (with three-day-total rainfall of more than 1400 mm), strong wind gusts, fresh flood, and caused severe economical and societal damage, including 92 human lives (Sui et al. 2002). Precipitation efficiency of Typhoon Nari over the ocean was discussed in Sui et al. (2005), and the flooding simulation of Nari was examined in Li et al. (2005). Yang et al. (2008; hereafter referred to as Part I) conducted a quadruply nested-grid MM5 model simulation with the finest grid size of 2 km for Nari and showed that the model reproduces reasonably well the kinematic and precipitation features as well as the structural changes of Nari, as verified against radar and rain-gauge observations. These include the storm track, contraction and sizes of the eye and eyewall, the spiral rainbands, the rapid pressure rise (~1.67 hPa h^{-1}) during landfall, and the nearly constant intensity after landfall. In addition, the model captures the horizontal rainfall distribution and some local rainfall maxima associated with Taiwan's orography. Through a series of terrain sensitivity experiments, Part I found that the impact of island terrain on Nari's intensity is nearly linear, with stronger storm intensity but less rainfall amounts in lower-terrain runs. In contrast, changing the terrain heights produces nonlinear tracks, with "circled" shapes and variable movements due to different degrees of blocking effects.

---

*Corresponding author address: Prof. Ming-Jen Yang, Department of Atmospheric Sciences, National Central University, Chung-Li, 320, Taiwan. E-mail: mingjen@cc.ncu.edu.tw

In order to further understand the evolution of tangential and radial flows of Typhoon Nari upon its landfall on Taiwan, absolute angular momentum (AAM) and radial wind budgets of Nari are conducted by analyzing the MM5 model outputs from Part I with high spatial and temporal resolutions (2-km horizontal grid size and 2-min output interval). Before landfall, Nari's tangential flow exhibits an evident wavenumber-1 signature, with radial inflow at low levels and outflow at upper levels (see Figs. 12 and 16 of Part I). After landfall, the horizontal wind field becomes highly asymmetric (see Figs. 13 and 15 of Part I). Both radar observation and MM5 simulation indicate that the radial inflow at low levels becomes thicker and stronger, and the sloping radial outflow jet is maximized at middle levels over the rugged terrain.

The first objective of this study is to investigate the evolution of tangential and radial flows of Nari during its landfall on Taiwan, especially for the transition from the more axisymmetric structure over the ocean to the highly-asymmetric features over mountains. The second objective is to understand the extent that the GWB is still valid for a landfalling TC. The third purpose is to examine the physical mechanism responsible of the sloping mid-level radial outlflow over the topography. Through the analyses of AAM and radial momentum budgets, we wish to gain insight into how the balanced and unbalanced flows are generated and distributed as Nari encountered the mountainous topography in Taiwan.

2. METHODOLOGY

All momentum budget calculations are based on the governing equations used in the PSU-NCAR MM5 model (Dudhia 1993; Grell et al. 1995). Following ZLY, because of the axisymmetric nature of TCs, we also discusses the inner-core dynamics of Nari in the cylindrical coordinate (r, λ, z), where r is the radius from the TC center pointing outward, λ is the azimuthal angle, and z is the vertical height axis.

The governing equation in the cylindrical coordinate for the radial wind can be written as

$$\frac{dU}{dt}=-\frac{1}{\rho}\frac{\partial p}{\partial r}+\frac{V^2}{r}+fV-2\Omega\cos\phi W\cos\lambda+U_D, \quad (1)$$

where

$$\frac{d}{dt}=\frac{\delta}{\delta t}+U'\frac{\partial}{\partial r}+\frac{V'}{r}\frac{\partial}{\partial\lambda}+W\frac{\partial}{\partial z}\,; \quad (2)$$

W, U, and V are the vertical, radial and tangential (azimuthal) winds relative to the earth in the cylindrical coordinate; Ω is the angular velocity of the earth; and ϕ is the latitude. To separate the translation effect from storm's dynamical processes, we define $\delta/\delta t=\partial/\partial t+C\cdot\nabla$ as the local tendency, where ***C*** is the TC's motion velocity, and U' and V' are the horizontal wind components relative to the storm. Equation (1) states that the radial acceleration is determined by the radial pressure gradient force (PGF$_R$; U_P), the centrifugal force (U_E), the Coriolis force (U_C) including the effects of vertical motion, and the effects of the MBL and turbulent mixing (U_D). Note that the sign error for the Coriolis effect by vertical motion in ZLY has been corrected in Eq. (1).

The governing equation for the tangential wind in the cylindrical coordinate can be written as

$$\frac{dV}{dt}=-\frac{1}{\rho}\frac{\partial p}{r\partial\lambda}-\frac{UV}{r}-fU+2\Omega\cos\phi W\sin\lambda+V_D. \quad (3)$$

As in ZLY, it is more meaningful physically to rewrite Eq. (3) in terms of the AAM as defined by

$$M=r(V+\frac{fr}{2})\,, \quad (4)$$

with the form

$$\frac{dM}{dt}=-\frac{1}{\rho}\frac{\partial p}{\partial\lambda}-2r\Omega\cos\phi W\sin\lambda+\frac{r^2}{2}v_m\beta+rV_D\,, \quad (5)$$

where β is the variation of the Coriolis parameter with latitude and v_m is the projections of U and V into the longitudinal axes. Equation (5) indicates that the Lagrangian derivative of AAM results from a pressure torque, a longitudinally-oriented Coriolis torque by the vertical motion, a beta torque, and a torque due to the MBL effect and turbulent mixing process. Note that the sign error for the longitudinally-oriented Coriolis torque by the vertical motion in ZLY has been corrected in Eq. (5).

For Typhoon Nari, all the budget terms above are directly obtained from the MM5 outputs over the finest 2-km grid at 2-min intervals from the 13–14-h (valid at 0100–0200 UTC 16 Sept) and 22–23-h (valid at 1000–1100 UTC 16 Sept 2001) integrations, respectively. For the period of 0100–0200 UTC 16 Sept, which is 9 h prior to landfall, the storm is still intensifying (see Fig. 5 of Part I). For the period of 1000–1100 UTC 16 Sept, it is the first one-hour period after storm's landfall (the simulated Nari makes landfall on Taiwan at 1000 UTC 16 Sept 2001; see Fig. 4 of Part I). Each variable is transformed from the MM5 model coordinate (x, y, σ) to the cylindrical coordinate (r, λ, z) with the typhoon center at the origin. The earth-relative local tendency term ($\partial/\partial t$) is calculated using the second-order central differencing with a time interval of 2 min. The terms for MBL effect and turbulent mixing process (U_D and V_D) are calculated as the residues from other terms in Eqs. (1) and (3); thus numerical errors are included in these terms as well. For results presented in the next section, each budget term is averaged azimuthally (for each 2-min dataset) and temporally over the two 1-h periods. The horizontal winds relative to the storm are obtained by subtracting out the storm's movement at an eastnortheasterly speed of 14 m s^{-1} at the 13–14-h period and a northeasterly speed of 11 m s^{-1} at the 22–23-h period, respectively (see Table 1 and Fig. 4 of Part I).

For the convenient of subsequent discussion, Fig. 1 shows the radius-height cross sections of the temporally and azimuthally averaged tangential (V') and radial (U') flows, vertical velocity (W), and AAM of Nari while it is still over ocean. In general, it displays the typical kinematic and AAM features of an oceanic TC at its intensifying-to-mature stage (see Fig. 1 of ZLY). The mean axisymmetric tangential flow exhibits a ring of intense flow (V'_{max} = 57 m s^{-1}) maximized at a radius of 20 km and an altitude of 1 km (Fig. 1a). The axis of RMW (labeled as R in Fig. 1a) lies outside the slantwise updrafts (labeled as U in Fig. 1c) in the eyewall and slopes outward with height up to 12 km. The surface friction causes strong vertical wind shear in the MBL (for levels below 1–1.5 km in Fig. 1a). The low-level inflow, peaked (> 14 m s^{-1}) at the surface near r = 30 km, turns sharply upward into the deep updrafts in the eyewall (Fig. 1c) and the outflow jet (> 7 m s^{-1}) at upper levels peaked near 12 km (Fig. 1b). In the outer rainband region (r > 50 km), there are mid-level radial inflow sloping downward to the inner-core region, associated with the latent cooling by sublimation and melting [see Figs. 6 and 7 of Yang (2008)]. Dynamically-induced downdrafts (labeled as D in Fig. 1c) occurs at the interface between the eye and eyewall, and mesoscale updrafts with weaker magnitude but broader horizontal size are located above the melting level in the outer rainband region (see Fig. 14 of Part I for the vertical position of the melting level). The mean AAM shows significant inward decreases with a large vertical gradient in the MBL by surface friction and outward increases in upper outflow layers by radial advection (Fig. 1d). The secondary-circulation flow vectors follow closely the AAM surfaces within the eyewall (r = 10–30 km). As indicated by ZLY, the inward "buckling" of AAM in the vicinity of V'_{max} plays an important role in the spinup of the eyewall.

Figure 2 displays the temporally and azimuthally averaged kinematic and AAM structures during the first one-hour period after storm's landfall on Taiwan. Although the general features in Fig. 2 are similar to those in Fig. 1, there are several noticeable features needed to be mentioned. Note that after transforming from the MM5 model coordinate (x, y, σ) to the cylindrical coordinate (r, λ, z), data beneath the mountain are not included in the azimuthal average. The vertical axis of RMW is tilted outward with height below 2 km (Fig. 2a), due to the retardation of tangential flow by Mt. Snow (also see Fig. 15c in Part I). The low-level inflow is increased to reach the peak magnitude of 25 m s^{-1}, due to the enhanced friction by Taiwan topography (Fig. 2b). The mid-level radial outflow in the inner-core region becomes much stronger (U'_{max} = 12 m s^{-1} in Fig. 2b), compared to that prior to landfall ($U'_{max} \leqq$ 2 m s^{-1} in Fig. 1b); similar features are also shown in the along-track cross section (see Fig. 16c in Part I). Updrafts in the eyewall are peaked at a lower altitude and show a distinct multicelluar structure after landfall (Fig. 2c). The AAM surfaces are tilted further outward vertically in the inner-core region (r = 20–50 km) and the "buckling height" of the AAM surface occurs at higher altitude in outer region (r > 40 km), indicating the rapid spindown of tangential flow due to the enhanced retardation and surface friction by the topography (Fig. 2d).

3. AAM AND RADIAL MOMENTUM BUDGETS: AXISYMMETRIC STRUCTURE

Figure 3 shows the AAM budget terms of Typhoon Nari prior to landfall, which are similar to those in Hurricane Andrew (see Fig. 2 of ZLY). The Lagrangian tendency (dM/dt; Fig. 3a) represents the sources/sinks of AAM associated with turbulent mixing (mainly in the interface between the eye and eyewall) and surface friction (mainly within the MBL), since the pressure torque almost vanishes after the azimuthal average and the other two terms on the right-hand side of Eq. (5) are very small. Turbulent mixing decreases the local AAM within the eyewall and increases AAM inward to the eye; the MBL (below 1–2 km) is a sink of AAM as the result of frictional dissipation. Above the MBL, AAM is nearly conserved with very small Lagrangian tendency. The horizontal advection of AAM (M_H; Fig. 3b) is in opposite sign to the vertical advection of AAM (M_V; Fig. 3b) at the inner edge of eyewall (r = 10–20 km), as expected from the conservation of AAM. Similar out-of-phase relationship between the horizontal advection and vertical advection for horizontal momentum is indicated by Yang and Houze (1996) for deep convection within a squall-line system. The radial inflow in the MBL increases the AAM of the storm by transporting the high-AAM air mass at the outer region inward (Fig. 3b), and the vertical advection transports the AAM upward in the eyewall and outward in the upper outflow layer (Fig. 3c). The net result is that the local AAM tendency above the MBL is a small residue between horizontal and vertical advections (Fig. 3d). The updraft axis in the eyewall (labeled by U) corresponds to negative AAM tendency, indicating the slow spindown of tangential flow at a later time.

Figure 4 illustrates all the radial budget terms in Eq. (1) and the extent of different balanced-wind approximations when Nari is still over ocean. The most intense PGF_R (U_P) occurs in the eyewall and its axis follows closely that of the RMW (labeled as R; see Figs. 1a and 4a). This negative PGF_R decreases rapidly with height and accounts for the generation of radial inflow in the MBL that increases toward the

RMW. The centrifugal force (U_E) has similar structure but opposite sign to the PGF_R (Fig. 4b). The sum of these two terms denotes the degree of cyclostrophic force imbalance ($U_{PE} = U_P + U_E$; Fig. 4c). For the eye and the inner edge of eyewall (r < 20 km), U_E overcompensates U_P, which results in strong supercyclostrophic accelerations ($U_{PE} > 0$); on the other hand, small subcyclostrophic accelerations ($U_{PE} < 0$) occur at the outer edge of eyewall and outer rainband regions. The degree of gradient wind imbalance ($U_{PEC} = U_{PE} + U_C$) is shown in Fig. 4d. Because U_C is very small compared to the maximum value of U_P or U_E, the distribution of gradient wind imbalance (U_{PEC}) is very similar to that of cyclostrophic force imbalance (U_{PE}). After including U_C, the positive (outward) accelerations are more significant for the flow above the MBL in the eye and the inner edge of eyewall, indicating evident supergradient tendencies ($U_{PEC} > 0$). The effects of MBL, turbulent mixing, and numerical errors on radial momentum are shown in Fig. 4e. The positive acceleration near the surface within the MBL indicates the slowdown of radial inflow by surface friction; strong turbulent mixing in the eye and the inner edge of eyewall (r < 20 km) also act to spindown the radial outflows at mid-to-upper levels. The net Lagrangian acceleration (Fig. 4f) has similar features to those of the gradient wind imbalance (Fig. 4d), except for the MBL where the centrifugal "braking effect" on the radial inflow is enhanced (see Fig. 6 of ZLY).

One-hour after Nari's landfall on Taiwan, the radial flows have pronounced changes (cf Figs. 1b and 2b), and the budget terms in Fig. 5 are used to explain the mechanisms responsible for the change of radial flows. The negative PGF_R (U_P) still indicates inward acceleration, and decreases rapidly with height (Fig. 5a); its peak value is decreased (–500 vs. –600 $m^2\ s^{-1}\ h^{-1}$) after landfall as a result of weaker storm intensity. On the other hand, the centrifugal force (U_E) remains similar maximum magnitude (650 $m^2\ s^{-1}\ h^{-1}$) to that prior to landfall (Fig. 5b). Strong supercyclostrophic accelerations ($U_{PE} > 0$) occur in the eye and the inner edge of eyewall (for radius less than 30 km), and small subcyclostrophic accelerations ($U_{PE} < 0$) are located below the MBL at the outer edge of inner-core region (r = 30–60 km; Fig. 5c). The pattern of gradient wind imbalance (U_{PEC}) is still very similar to that of cyclostrophic force imbalance (U_{PE}), even after storm's landfall. Supergradient accelerations ($U_{PEC} > 0$) are pronounced for the flow above the MBL in the eye and eyewall, and again small subgradient accelerations ($U_{PEC} < 0$) are located near the surface in outer region (r = 30–60 km; Fig. 5d). The axis of supergradient acceleration at the middle levels in the inner core (for r = 20–50 km and z = 2–5 km in Fig. 5d) is tiled outward with height, which is collocated with the axis of mid-level radial outflow (Fig. 2b). The detailed analysis of radial-wind advection terms indicates that the vertical transport of radial inflow into the middle level is responsible for this supergradient acceleration (figure not shown). Figure 5e shows negative radial accelerations by mixing and diffusion in the eye and the inner edge of eyewall (r < 20 km) and positive radial accelerations by friction near the surface. The net Lagrangian acceleration in Fig. 5f displays positive radial acceleration at middle levels (r < 40 km and z < 4 km) and negative acceleration near the surface (r = 30–80 km).

In summary, from the diagnostics of AAM budget, we find that after landfall the tangential wind is decreased at low levels through the upward transport of weaker tangential wind and further reduced by friction and turbulence with the boundary layer. It is determined from the radial budget that the centrifugal force (U_E) is greater than the pressure gradient force (U_P), leading to supergradient winds over Taiwan's topography. The radial inflow at low levels becomes stronger and thicker after landfall, resulting from the vertical transport of stronger radial inflow upward. Both centrifugal and pressure gradient forces contribute to the radially-outward acceleration, resulting in the sloping radial outflow jet at middle levels over the mountain.

Finally, Figs, 2 and 5 only discuss the axisymmetric structures of kinematic feature, AAM, and radial momentum budgets of Typhoon Nari for the first hour after its landfall. However, the rugged terrain of Mt. Snow imposes significant asymmetries on Nari's primary and secondary circulations. More details of the terrain-induced asymmetries on Nari's kinematic fields will be given during the oral presentation at the conference.

Reference

Dudhia, J. 1993: A nonhydrostatic version of the Penn State/NCAR mesoscale model: Validation tests and simulation of an Atlantic cyclone and cold front. *Mon. Wea. Rev.*, **121**, 1493–1513.

Emanuel, K. A., 1986: An air-sea interaction theory for tropical cyclones. Part I: Steady state maintenance. *J. Atmos. Sci.*, 43, 585–604.

Gray, W. M., and D. J. Shea, 1973: The hurricane inner core region: Thermal stability and dynamic characteristics. *J. Atmos. Sci.,* **30**, 1565–1576.

Grell, G. A., J. Dudhia, and D. R. Stauffer, 1995: A description of the fifth-generation Penn State/NCAR Mesoscale Model. NCAR Technical Note, 138 pp.

LaSeur, N. E., and H. F. Hawkins, 1963: An analysis of Hurricane Cleo (1958) based on data from research reconnaissance aircraft. *Mon. Wea. Rev.*, **91**, 694-709.

Li, M.-H., M.-J. Yang, R. Soong, and H.-L. Huang**,** 2005: Simulating typhoon floods with gauge data and mesoscale modeled rainfall in a mountainous watershed. *J. Hydrometeor*., **6**, 306–323.

Liu, Y., D.-L. Zhang, and M. K. Yau, 1997: A multiscale numerical study of Hurricane Andrew (1992). Part I:

Explicit simulation and verification. *Mon. Wea. Rev.*, **125**, 3073–3093.

Liu, Y., D.-L. Zhang, and M. K. Yau, 1999: A multiscale numerical study of Hurricane Andrew (1992). Part II: Kinematics and inner-core structures. *Mon. Wea. Rev.*, **127**, 2597–2616.

Schubert, W. H., and J. J. Hack, 1983: Transformed Eliassen-balanced vortex model. *J. Atmos. Sci.*, **40**, 1571–1583.

Shapiro, L. J., and H. E. Willoughby, 1982: The response of the balanced hurricanes to local sources of heat and momentum. *J. Atmos. Sci.*, **39**, 378–394.

Sui, C.-H., and Co-authors, 2002: Typhoon Nari and Taipei flood—A pilot meteorology-hydrology study. EOS, Transctions, *Amer. Geophy. Union*, **83**, 265, 268–270.

Sui, C.-H., X. Li, M.-J. Yang, and H.-L. Huang**,** 2005: Estimation of oceanic precipitation efficiency in cloud models. *J. Atmos. Sci.*, **62**, 4358–4370.

Willoughby, H. E., 1990: Gradient balance in tropical cyclones. *J. Atmos. Sci.*, **47**, 265–274.

Willoughby, H. E., 1991: Reply. *J. Atmos. Sci.*, **48**, 1209–1212.

Yang, M.-J., 2008: A microphysical processes of Typhoon Nari (2001) at landfall. *Preprints, The 28th Conference on Hurricane and Tropical Meteorology*, Orlando, FL, 28 April to 2 May 2008, Amer. Meteor. Soc., 12C.5.

Yang, M.-J., and R. A. Houze, Jr., 1996: Momentum budget of a squall line with trailing stratiform precipitation: Calculations with a high-resolution numerical model. *J. Atmos. Sci.*, **53**, 3629–3652.

Yang, M.-J., D.-L. Zhang, and H.-L. Huang, 2008: A modeling study of Typhoon Nari (2001) at landfall. Part I: The topographic effects. *J. Atmos. Sci.*, **65**, 3095-3115.

Zhang, D.-L., Y. Liu, and M. K. Yau, 2000: A multiscale numerical study of hurricane Andrew (1992). Part III: Dynamically induced vertical motion. *Mon. Wea. Rev.*, **128**, 3772–3788.

Zhang, D.-L., Y. Liu, and M. K. Yau, 2001: A multiscale numerical study of Hurricane Andrew (1992). Part IV: Unbalanced Flows. *Mon. Wea. Rev.*, **129**, 92–107.

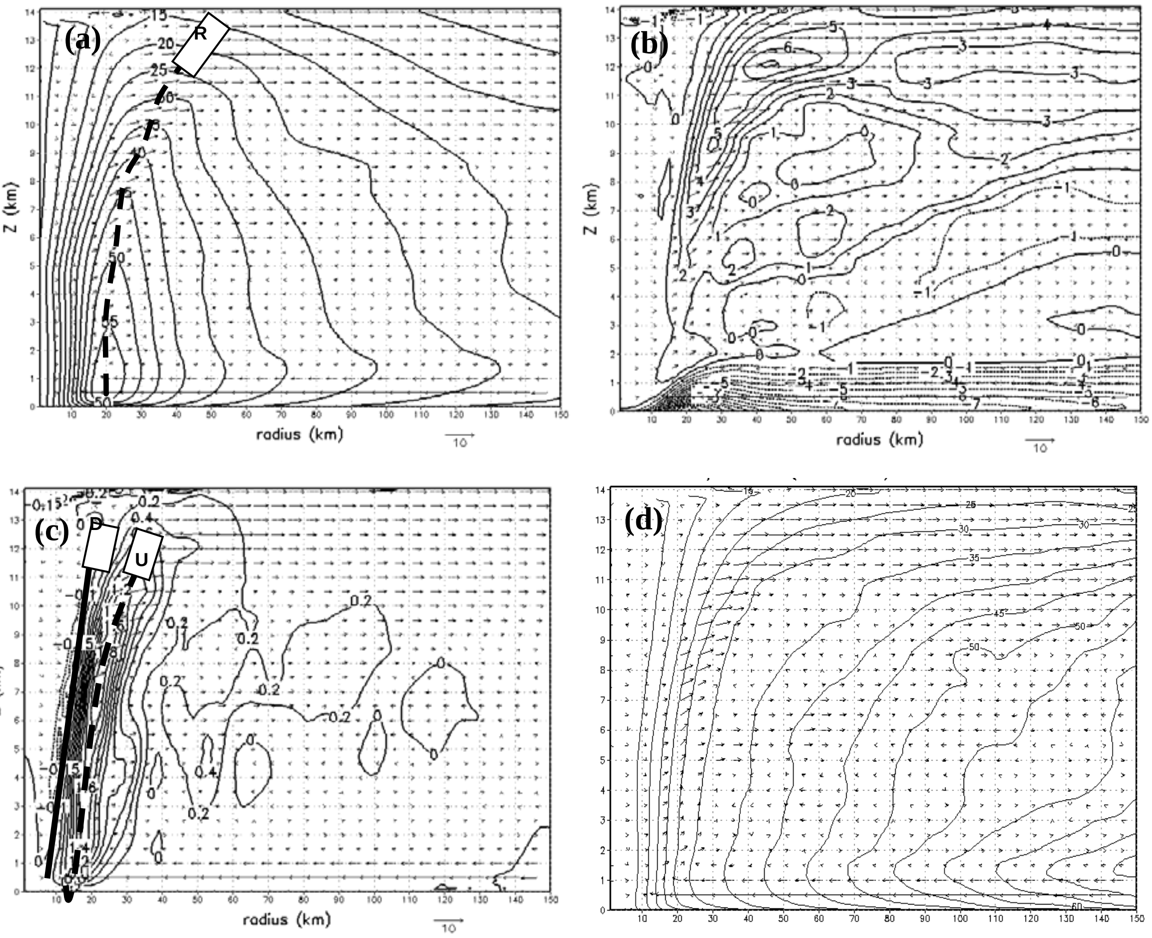

Figure 1: Radius-height cross sections of the hourly- and azimuthally-averaged (a) tangential winds (*V'*) at intervals of 5 m s^{-1}, (b) radial winds (*U'*) at 1 m s^{-1}, (c) vertical velocity (*W*) at intervals of 0.2 m s^{-1}, and (d) absolute angular momentum (AAM) at intervals of 5 x 10^{5} m^{2} s^{-1} of Typhoon Nari, superposed with the cross-sectional flow vectors, taken from the 13-14 h integration or the period of 0100-0200 UTC 16 Sept 2001. Horizontal winds at (a) and (b) are storm-relative. The radius of maximum wind, the axes of the eyewall updrafts and the inner-edge downdrafts are represented by R, U, and D, respectively.

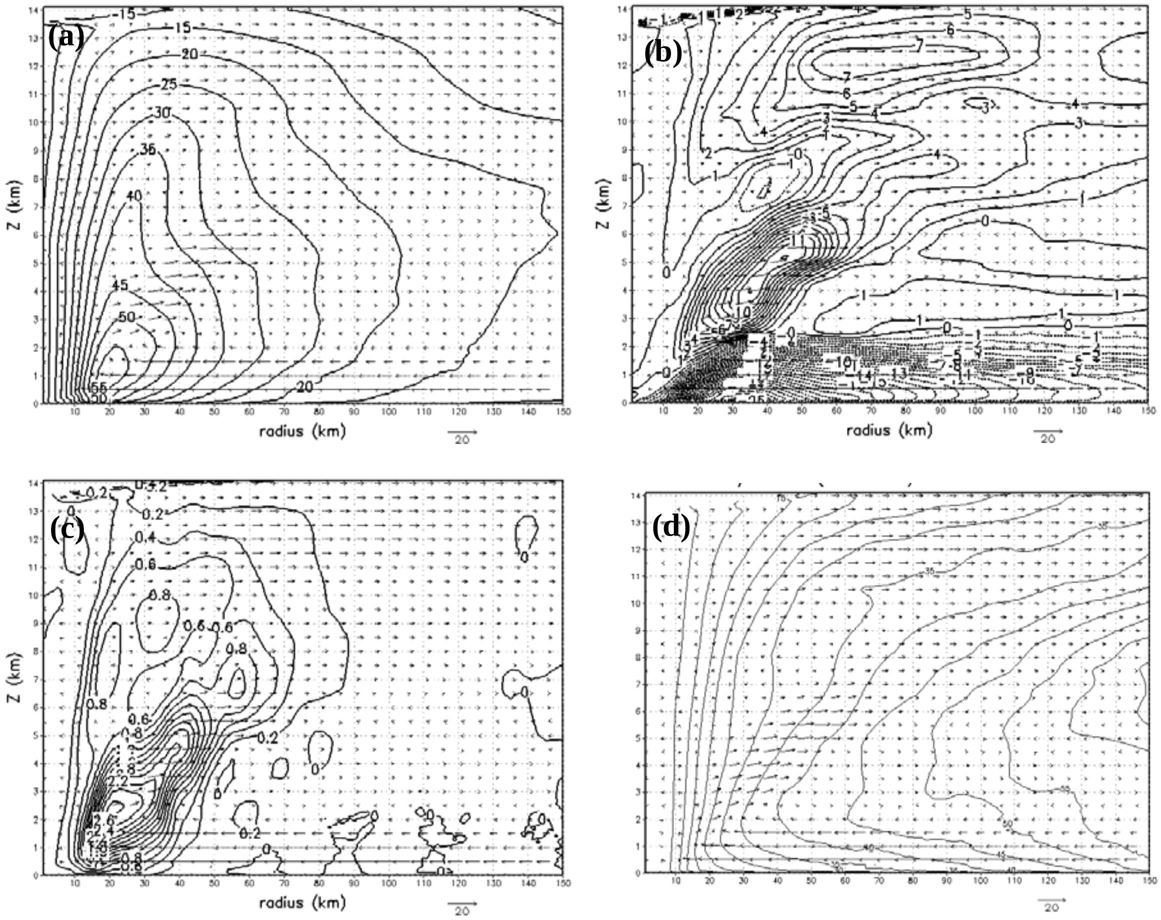

Figure 2: As in Fig. 1 but for the hourly- and azimuthally-averaged kinematic and AAM fields of Typhoon Nari taken from the 22-23 h integration or the period of 1000-1100 UTC 16 Sept 2001. Horizontal winds at (a) and (b) are storm-relative. Contour intervals are 5 m s^{-1} in (a), 1 m s^{-1} in (b), 0.2 m s^{-1} in (c), and 5 x 10^5 m^2 s^{-1} in (d), respectively.

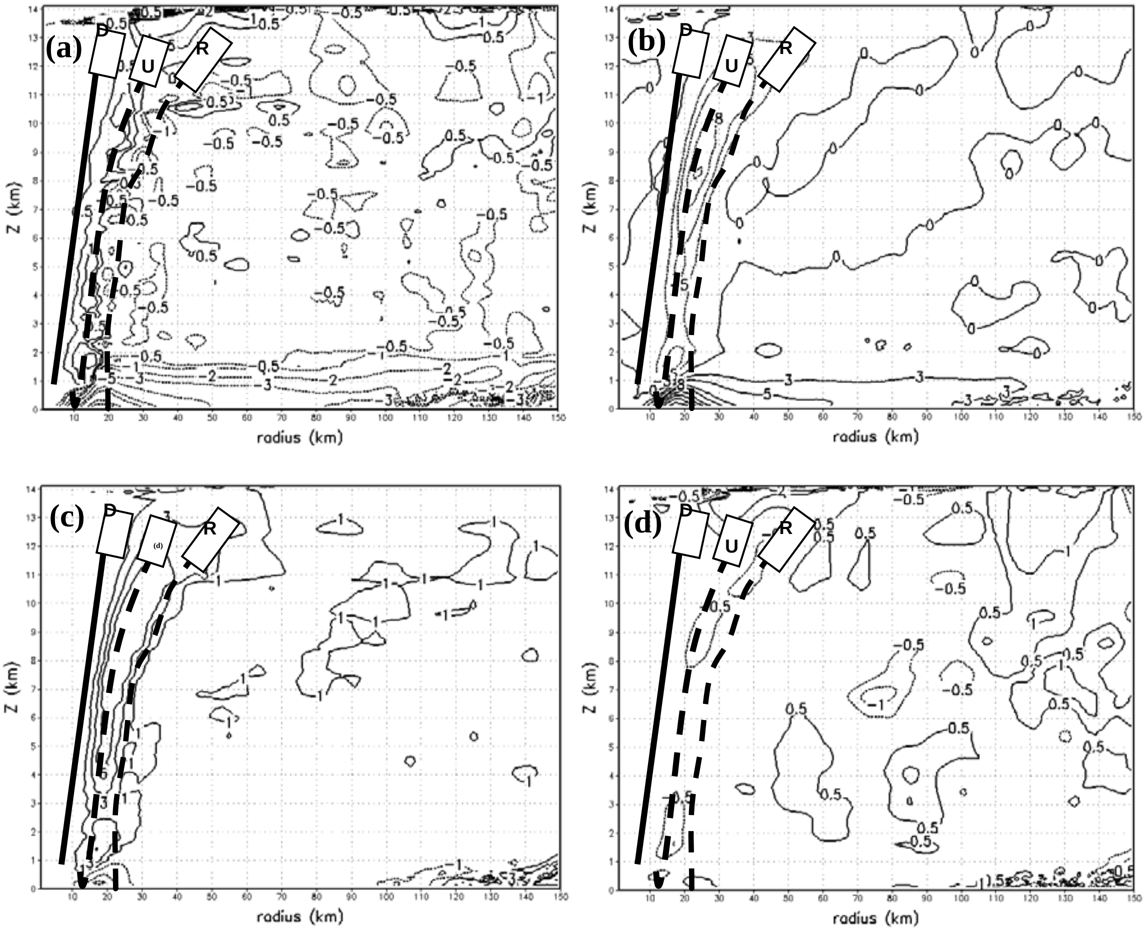

Figure 3: As in Fig. 1 but for the hourly- and azimuthally-averaged AAM budget of Typhoon Nari: (a) the net Lagrangian tendency due to all the sources/sinks (*dM/dt*), (b) the horizontal advection (M_H), (c) the vertical advection (M_V), and (d) the local tendency (M_t). (a) is contoured at ±0.5, ±1, ±2, ±3, ±5, ±8, ±10, ±16, ±20, and ±25 × 10^5 m^2 s^{-1} h^{-1}; (b) is contoured at 0, ±3, ±5, ±8, ±10, ±13, ±16, ±20, and ±25 × 10^5 m^2 s^{-1} h^{-1}; (c) is contoured at ±1, ±3, ±5, ±10, ±16, ±20, and ±25 × 10^5 m^2 s^{-1} h^{-1}; (d) is contoured at ±0.5, ±1, and ±2 × 10^5 m^2 s^{-1} h^{-1};

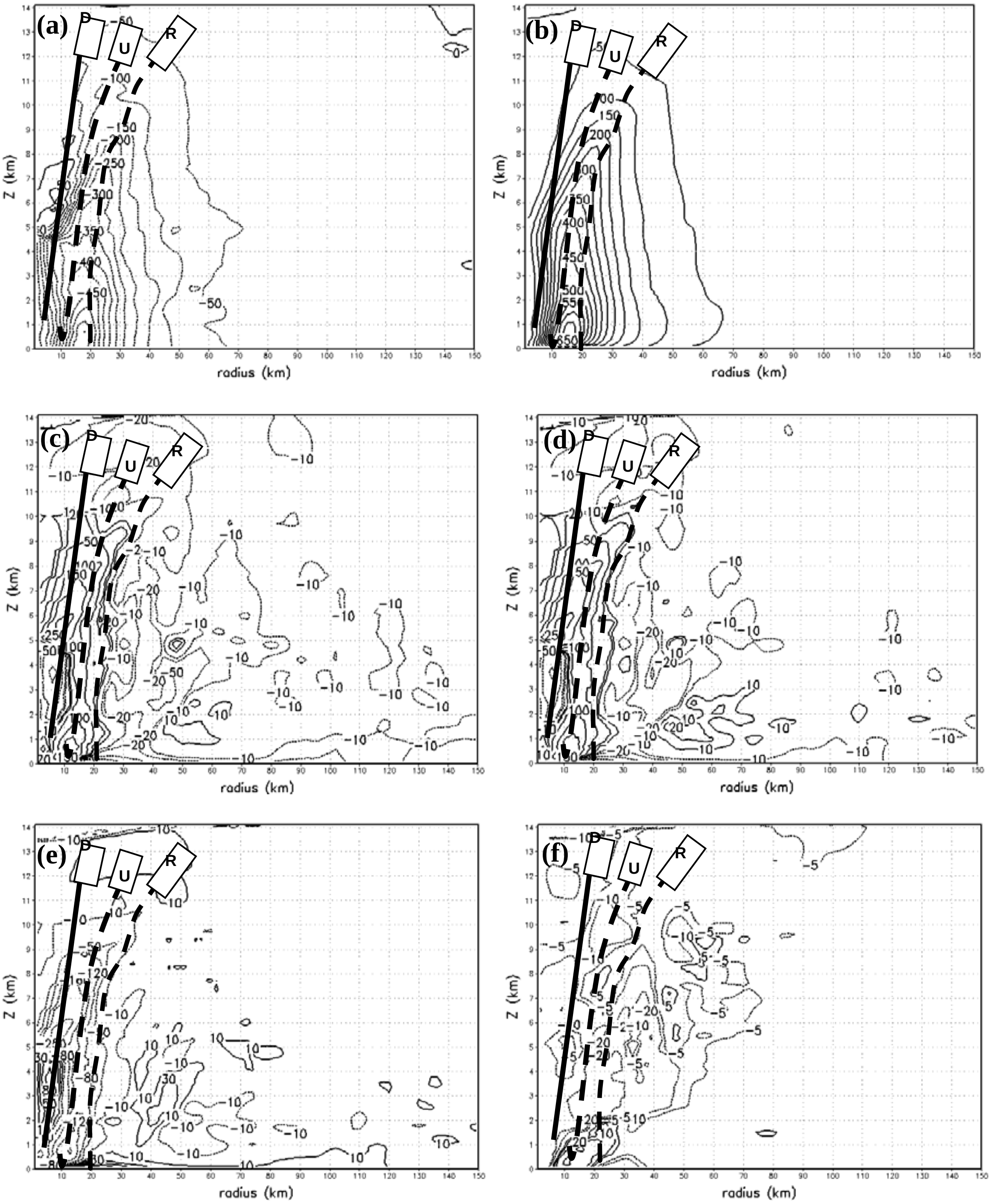

Figure 4: As in Fig. 1 but for the hourly- and azimuthally-averaged radial momentum budget of Typhoon Nari: (a) the radial pressure gradient force (PGF_R, U_P), (b) the centrifugal force (U_E), (c) the cyclostrophic force imbalance ($U_{PE} = U_P + U_E$), (d) the gradient-force imbalance ($U_{PEC} = U_{PE} + U_C$), (e) the diffusion and boundary layer effects (U_B), and (f) the Lagrangian tendency (dU/dt). Both (a) and (b) are contoured at intervals of 50 $m^2\ s^{-1}\ h^{-1}$; both (c) and (d) are contoured at ±10, ±20, ±50, ±100, ±150, and ±250 $m^2\ s^{-1}\ h^{-1}$; (e) is contoured at ±10, ±30, ±50, ±80, ±120, ±160 and ±250 $m^2\ s^{-1}\ h^{-1}$; (f) is contoured at ±5, ±10, ±20, ±50, ±70, ±100, ±160 and ±250 $m^2\ s^{-1}\ h^{-1}$.

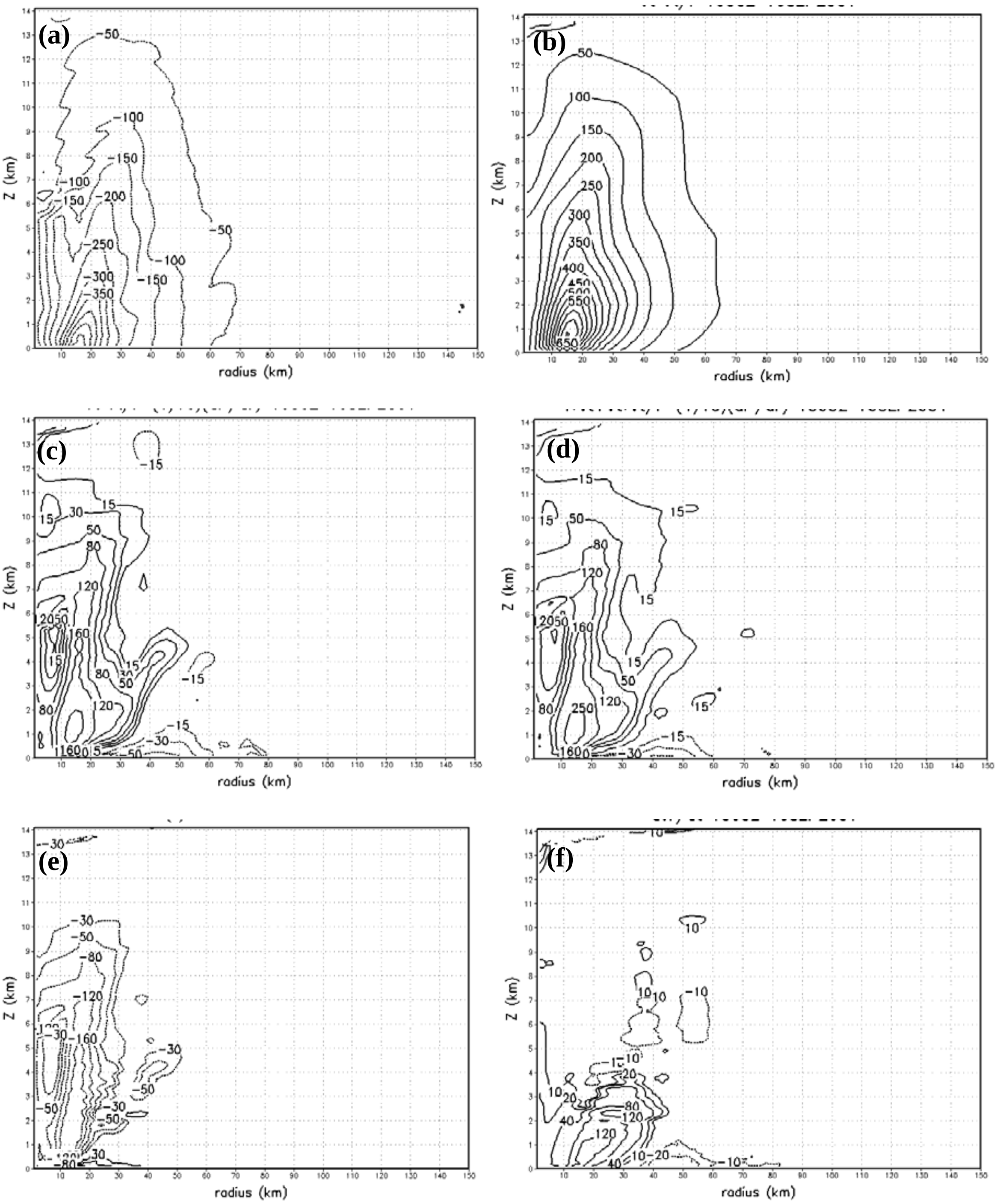

Figure 5: As in Fig. 4 but for the radial momentum budget of Typhoon Nari taken from the 22-23 h integration or the period of 1000-1100 UTC 16 Sept 2001: (a) the radial pressure gradient force (PGF_R, U_P), (b) the centrifugal force (U_E), (c) the cyclostrophic force imbalance ($U_{PE} = U_P + U_E$), (d) the gradient-force imbalance ($U_{PEC} = U_{PE} + U_C$), (e) the diffusion and boundary layer effects (U_B), and (f) the Lagrangian tendency (dU/dt). Both (a) and (b) are contoured at intervals of 50 $m^2 s^{-1} h^{-1}$; both (c) and (d) are contoured at ±15, ±30, ±50, ±80, ±120, ±160, and ±250 $m^2 s^{-1} h^{-1}$; (e) is contoured at ±30, ±50, ±80, ±120, ±160 and ±250 $m^2 s^{-1} h^{-1}$; (f) is contoured at ±10, ±20, ±40, ±80, ±120, ±160 and ±250 $m^2 s^{-1} h^{-1}$.